Harmonic Suppression Based on Rectified Current Regulation With DC-Link Voltage Decoupling for Electrolytic Capacitorless PMSM Drives

Dawei Ding, *Member, IEEE*, Hui Xie, Binxing Li, *Member, IEEE*, Gaolin Wang, *Senior Member, IEEE*, Runfeng Gao, Zekun Ren, Weixin Yue, and Dianguo Xu, *Fellow, IEEE*

***Abstract*—Harmonics suppression for grid currents is a key issue in electrolytic capacitorless permanent magnet synchronous motor drives. In this article, a strategy based on rectified current regulation with dc-link voltage decoupling (RCR-DVD) is proposed to enhance the harmonics suppression performance of grid currents. The small-signal model of the drive with RCR is built to reveal the disturbance caused by the dc-link voltage and digital control delay, which may reduce the harmonics suppression capability and lead to stability issue. Then, the RCR-DVD is proposed to decouple the voltage disturbances from rectified current control loop for better harmonics suppression performance. Specifically, the voltage decoupling is realized by main harmonics prediction and proportional resonance controllers. The amplitude of grid-side input impedance can be increased compared with RCR, which means lower grid current harmonics. Experimental results validate the effectiveness of the proposed method.**

***Index Terms*—DC-link voltage decoupling, electrolytic capacitorless, permanent magnet synchronous motor (PMSM), rectified current regulation (RCR).**

I. Introduction

PERMANENT magnet synchronous motor (PMSM) has been widely applied in electric vehicles, industrial manufacturing, and home appliances because of its high efficiency and high power density [1], [2], [3], [4]. The electrolytic capacitorless motor drives with slim film capacitors can significantly improve the power density and reliability, which have been commonly used in the heating, ventilation, and air conditioning (HVAC) with power ratings ranging from 2.5 to 45 kW [5], [6].

Manuscript received 11 July 2023; revised 16 October 2023; accepted 12 November 2023. Date of publication 28 November 2023; date of current version 22 December 2023. This work was supported in part by the Research Fund for the National Natural Science Foundation of China under Grants 52207042 and 52125701, in part by the grant from the Delta Power Electronics Science and Education Development Program of Delta Group (DREG2023005), in part by the Fellowship of China Postdoctoral Science Foundation (2022M720946), and in part by the Financial Assistance under Heilongjiang Postdoctoral Fund (LBH-Z220022). Recommended for publication by Associate Editor M. Hartmann. *(Corresponding author: Binxing Li.)*

The authors are with the School of Electrical Engineering and Automation, Harbin Institute of Technology, Harbin 150001, China (e-mail: dingdawei@hit.edu.cn; 22s106178@stu.hit.edu.cn; lbx@hit.edu.cn; wgl818@hit.edu.cn; 1160800915@stu.hit.edu.cn; 22b906014@stu.hit.edu.cn; 23b906041@stu.hit.edu.cn; xudiang@hit.edu.cn).

Color versions of one or more figures in this article are available at https://doi.org/10.1109/TPEL.2023.3335150.

Digital Object Identifier 10.1109/TPEL.2023.3335150

However, the decrease of the dc-link capacitance leads to the energy coupling between the grid side and the motor side, which results in a decrease in the quality of grid currents. In order to improve the quality of grid currents in electrolytic capacitorless motor drives, a variety of power converter topologies have been proposed [7], [8], [9], [10]. These methods improve the quality of grid currents by adding hardware circuits, which lead to an increase in the cost and volume of the system. The algorithm-based resonance suppression method does not require the additional circuits, which has a better application prospect. At present, it has been successfully applied in grid-connected inverters, renewable energy generation systems, and electrolytic capacitorless motor drives to improve system stability and reduce the total harmonic distortion (THD) of grid currents [11], [12], [13]. The resonance suppression methods are mainly divided into active damping and negative impedance regulation.

The active damping method changes the characteristics of the system by paralleling virtual resistors, which has clear physical significance [14], [15], [16], [17], [18], [19]. In [14], a Luenberger observer was adopted to obtain the rectified voltage. The difference between the rectified voltage and the dc-link voltage was injected into the *d*-axis reference voltage, which is equivalent to parallel virtual resistors with the dc-link filter inductor. In [15], the possible configurations of damping resistor were analyzed to obtain the optimal solution. In order to realize the equivalent damping effect, the dc-link voltage feedback was applied to emulate the inductor current feedback-based active damping method. In [17], the angle and amplitude of the fluctuation component in the reference dc-link voltage were adjusted. The compensation impedance is related to the motor voltage, which improves the damping performance under different power levels. In [19], the 6th and 12th harmonics of the dc-link voltage extracted by a bandpass filter were injected into the motor current loop, which regulates the admittance and improves the stability of the system.

The motor fed by an inverter can be viewed as a constant power load (CPL) with negative impedance characteristics [18]. Varying the negative impedance characteristics can improve the stability of the motor drives and the quality of grid currents [20], [21], [22], [23], [24], [25]. In [20], a voltage feedback loop with time delay was established to make the equivalent admittance change into positive, which improves the system stability. In [22], a dc-link voltage controller was constructed, and its output

signal was added to the q-axis reference current together with the capacitor current, which suppresses the LC resonance. In [21], the fluctuations of the motor power were extracted and injected into the d-axis reference current, which increases the system damping and reduces torque ripples. In [23], a cascaded power and current control strategy was proposed to suppress the current pulsation, which can suppress current pulsation within a wide frequency range. In [24], the stability of the drive is improved by reconstructing the rectified voltage to extract the harmonic components amplified by the LC resonant circuit in the dc-link voltage.

These mentioned control methods can improve the quality of gird currents by changing the impedance of the system, which is indirect. In [26], the relationship between the rectified current and gird currents was investigated. As the harmonics of the rectified current increase, the THD of the gird currents also increases. Therefore, controlling the harmonics of the rectified current can improve the quality of grid currents directly. In [27], a method for suppressing harmonics in grid currents through rectified current regulation (RCR) was proposed. The rectified current was obtained by a current sensor. The relevant harmonics were extracted to inject into the dq-axis reference voltages. In [28], the rectified current was reconstructed based on the motor current without using the current sensor. The grid current control loop is independent from the speed and motor current control loops. However, the ideal control effect is difficult to achieve only using the proportional controller.

This article proposes a novel harmonics suppression method based on rectified current regulation with dc-link voltage decoupling (RCR-DVD) to achieve better quality of grid currents. Compared with the active damping control strategies mentioned above, the proposed strategy is a closed-loop control with better adaptability to operating conditions. The small-signal modeling method is applied to figure out the disturbances in RCR, which are caused by the fluctuated dc-link voltage and digital control delay. The harmonics suppression capability and system stability will decay due to the voltage disturbances. As a result, the RCR-DVD is proposed to decouple the voltage disturbances from the rectified current control loop to enhance the harmonics suppression performance and stability. According to the periodical characteristic of the dc-link voltage, the decoupling is realized by prediction and proportional resonance controllers. The grid-side input impedance is derived to evaluate the suppression ability on the 6th and 12th harmonics. The effectiveness of the proposed RCR-DVD is verified on a 5.5 kW electrolytic capacitorless PMSM experimental platform.

II. Limitations of Grid Current Harmonics Suppression Based on RCR

A. Modeling of RCR-Based Method

The topology of the three-phase electrolytic capacitorless PMSM drive system is shown in Fig. 1. In this system, the slim film dc-link capacitors are used instead of large volume electrolytic capacitors, which leads to energy coupling between the grid side and the motor side.

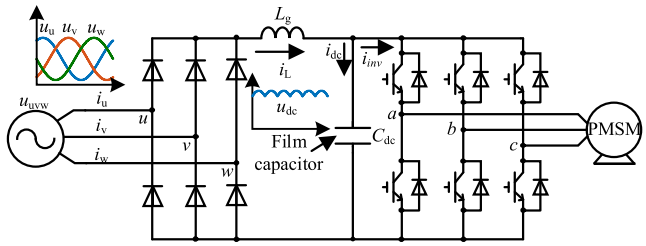

Fig. 1. Topology of the three-phase PMSM drive with slim film capacitors.

The output voltage of the rectifier u_{grec} can be represented as [29]

$$\begin{aligned} u_{\mathrm{grec}} &= u_0 + \sum_{n=1}^{\infty} a_{\mathrm{n}} \sin(6n\omega_{\mathrm{g}}t) + \sum_{n=1}^{\infty} b_{\mathrm{n}} \cos(6n\omega_{\mathrm{g}}t) \\ &= \frac{3\sqrt{6}}{\pi} U_{\mathrm{a}} + \sum_{n=1}^{\infty} -\frac{6\sqrt{6}U_{\mathrm{a}}\cos(n\pi)}{\pi(36n^2-1)} \cos(6n\omega_{\mathrm{g}}t) \end{aligned} \quad (1)$$

where u_0 is the dc component of the rectified voltage, n is a positive integer, ω_{g} is the angular frequency of the grid voltages, and U_{a} is the mean value of the phase voltages.

According to (1), it can be known that the rectified voltage contains a dc component and integer multiples harmonics of six times the grid frequency. The amplitude of the harmonics decreases when the frequency increases. At the frequency of LC resonance, the input impedance of the grid side is minimized, and the harmonics of the rectified voltage will excite the corresponding harmonics in the rectified current, thus decreasing the quality of grid currents. Considering the performance of the grid side and the effect of harmonics suppression, the resonance frequency is usually set to several hundred hertz [30]. Therefore, the rectified current can be regarded as mainly containing a dc component, a 6th harmonic, and a 12th harmonic [26].

For a three-phase PMSM drives with slim film capacitors, the 120° rectangular waveform is usually chosen as control target for grid currents. At this moment, the corresponding reference rectified current should be a dc waveform with the same magnitude as the reference grid currents. The THD of the 120° rectangular waveform is 29.7%, which is close to the theoretical minimum THD of grid currents in three-phase PMSM drives with slim film capacitors [28]. Therefore, eliminating the 6th harmonic component and 12th harmonic component in the rectified current can greatly improve the power quality of the grid currents.

The RCR uses the bandpass filter to extract the harmonics component from the rectified current, and the difference between the extracted and the reference value is inputted to the current proportional resonant controller. The output of the current controller is superimposed on the q-axis reference voltage to suppress the harmonics of the rectified current, thereby improving the quality of grid currents [27], [28]. The control block diagram of RCR is shown in Fig. 2.

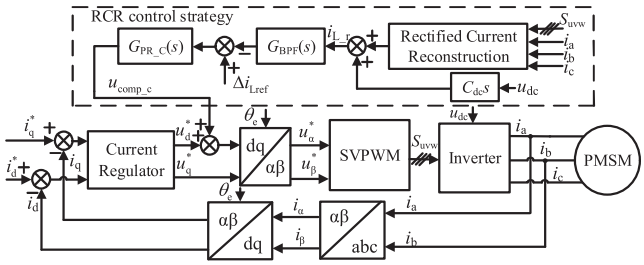

Fig. 2. Diagram of RCR control strategy.

B. Limitation of RCR

Typically, the inverter-controlled motor can be regarded as a CPL. However, when the control delay is considered, the motor will deviate from CPL characteristic [24]. To further improve the performance of RCR, the small-signal model, which considers the digital control delay, is established to analyze the intrinsic mechanism of RCR.

After applying RCR, the small-signal variations of *dq*-axis reference voltages $u_{\mathrm{d,qref}}$ can be expressed as

$$\begin{bmatrix}\Delta u_{\mathrm{dref}}(s)\\ \Delta u_{\mathrm{qref}}(s)\end{bmatrix} = \begin{bmatrix}-G_{\mathrm{d}}(s) & -\omega_{\mathrm{e}}L_{\mathrm{q}}\\ \omega_{\mathrm{e}}L_{\mathrm{d}} & -G_{\mathrm{q}}(s)\end{bmatrix}\begin{bmatrix}\Delta i_{\mathrm{d}}(s)\\ \Delta i_{\mathrm{q}}(s)\end{bmatrix} + \begin{bmatrix}0\\ -G_{\mathrm{BPF}}(s)G_{\mathrm{PR\_C}}(s)\Delta i_{\mathrm{L\_r}}(s)\end{bmatrix} \tag{2}$$

where L_{d} and L_{q} are the *dq*-axis inductances, $G_{\mathrm{d}}(s)$ and $G_{\mathrm{q}}(s)$ are the PI controllers for *d*-axis and *q*-axis currents, Δi_{d} and Δi_{q} are the small-signal variations of currents in *dq* axes, $\Delta i_{\mathrm{L\_r}}$ represents the small-signal variations of reconstructed rectified current, $G_{\mathrm{BPF}}(s)$ is the transfer function of the bandpass filter, and $G_{\mathrm{PR\_C}}(s)$ is the transfer function of the current proportional resonant controller, which can be expressed as

$$G_{\mathrm{PR\_C}}(s) = K_{\mathrm{RP\_C}} + \frac{2K_{\mathrm{RR\_C}}\omega_{\mathrm{c}}s}{s^2+2\omega_{\mathrm{c}}s+\omega_0^2} \tag{3}$$

where $K_{\mathrm{RP\_C}}$, $K_{\mathrm{RR\_C}}$, and ω_0 are the proportional coefficient, resonance coefficient, and the center frequency of resonant controller, respectively. ω_{c} is the bandwidth of the resonant controller that should be selected by considering the harmonics suppression effect and grid frequency deviation.

Considering the pulsewidth modulation (PWM) update and the delay in dc-link voltage sampling, there is a delay of 1.5 switching cycles in sampled dc-link voltage. Therefore, the small-signal variations of the *dq*-axis voltages $\Delta u_{\mathrm{d,q}}$ can be derived as

$$\begin{bmatrix}\Delta u_{\mathrm{d}}\\ \Delta u_{\mathrm{q}}\end{bmatrix} = e^{-1.5sT_{\mathrm{s}}}\begin{bmatrix}-G_{\mathrm{d}}(s) & -\omega_{\mathrm{e}}L_{\mathrm{q}}\\ \omega_{\mathrm{e}}L_{\mathrm{d}} & -G_{\mathrm{q}}(s)\end{bmatrix}\begin{bmatrix}\Delta i_{\mathrm{d}}(s)\\ \Delta i_{\mathrm{q}}(s)\end{bmatrix} + e^{-sT_{\mathrm{s}}}\begin{bmatrix}0\\ -G_{\mathrm{BPF}}(s)G_{\mathrm{PR\_C}}(s)\Delta i_{\mathrm{L\_r}}(s)\end{bmatrix} + \frac{\left(1-e^{-1.5sT_{\mathrm{s}}}\right)\Delta u_{\mathrm{dc}}}{U_{\mathrm{dc0}}}\begin{bmatrix}U_{\mathrm{dref0}}\\ U_{\mathrm{qref0}}\end{bmatrix} \tag{4}$$

where T_{s} is the sampling frequency, and $U_{\mathrm{d,qref0}}$ are the average value of the *dq*-axis reference voltages. Δu_{dc} and U_{dc0} are the small-signal variations and the average value of dc-link voltage, respectively.

According to the relationship shown in (A1), the transfer function between the $\Delta i_{\mathrm{d,q}}$ and Δu_{dc} can be expressed as

$$\begin{bmatrix}W_{\mathrm{dmad}}(s)\\ W_{\mathrm{qmad}}(s)\end{bmatrix} = \frac{1}{\Delta u_{\mathrm{dc}}}\begin{bmatrix}\Delta i_{\mathrm{d}}\\ \Delta i_{\mathrm{q}}\end{bmatrix} = \begin{bmatrix}W_{\mathrm{d}}(s)\\ W_{\mathrm{q}}(s)\end{bmatrix} + G_{\mathrm{mad}}(s)\frac{\Delta i_{\mathrm{L\_r}}}{\Delta u_{\mathrm{dc}}}\begin{bmatrix}A_{1\mathrm{q}}(s)\\ -A_{1\mathrm{d}}(s)\end{bmatrix} \tag{5}$$

where $W_{\mathrm{d,q}}(s)$ and $G_{\mathrm{mad}}(s)$ can be expressed as (A3) and (A4), which are shown in the Appendix. Due to the digital control delay caused by PWM calculation and update, there exists a switching delay in the output signal of the proportional resonant controller.

Neglecting the losses of the inverter, the small-signal variations of the inverter output power can be expressed as

$$\Delta u_{\mathrm{dc}}i_{\mathrm{inv0}} + U_{\mathrm{dc0}}\Delta i_{\mathrm{inv}} = 1.5\left(\Delta u_{\mathrm{d}}I_{\mathrm{d0}} + U_{\mathrm{d0}}\Delta i_{\mathrm{d}} + \Delta u_{\mathrm{q}}I_{\mathrm{q0}} + U_{\mathrm{q0}}\Delta i_{\mathrm{q}}\right) \tag{6}$$

where $I_{\mathrm{d,q0}}$ are *dq*-axis average currents, $U_{\mathrm{d,q0}}$ are *dq*-axis average voltages, and i_{inv0} and Δi_{inv} are the average value and small-signal variations of the inverter input current, respectively.

According to (5) and (6), the input impedance of the motor drive $Y_{\mathrm{mad}}(s)$ can be obtained as (7) shown at the bottom of the next page, where $Y_{\mathrm{mi}}(s)$ is the input impedance of the motor drive without control

$$Y_{\mathrm{mi}}(s) = -\frac{I_{\mathrm{inv0}}}{U_{\mathrm{dc0}}} + \frac{3W_{\mathrm{d}}(s)\left(U_{\mathrm{d0}}+\omega_{\mathrm{e}}L_{\mathrm{d}}I_{\mathrm{q0}}+L_{\mathrm{d}}I_{\mathrm{d0}}s+I_{\mathrm{d0}}R_{\mathrm{s}}\right)}{2U_{\mathrm{dc0}}} + \frac{3W_{\mathrm{q}}(s)\left(U_{\mathrm{q0}}-\omega_{\mathrm{e}}L_{\mathrm{q}}I_{\mathrm{d0}}+L_{\mathrm{q}}I_{\mathrm{q0}}s+I_{\mathrm{q0}}R_{\mathrm{s}}\right)}{2U_{\mathrm{dc0}}}. \tag{8}$$

Based on the model of the system, the small-signal block diagram of RCR is shown in Fig. 3, where $G_{\mathrm{K}}(s)$ is the transfer function between Δi_{inv} and Δi_{q}

$$G_{\mathrm{K}}(s) = \frac{\Delta i_{\mathrm{inv}}}{\Delta i_{\mathrm{q}}} = \frac{Y_{\mathrm{mad}}(s)}{W_{\mathrm{qmad}}(s)}. \tag{9}$$

As shown in Fig. 3, the input signals of the control loop are composed of the reference rectified current Δi_{Lref} and Δu_{dc}. Then, the open-loop transfer function of RCR can be expressed as

$$G_{\mathrm{L}}(s) = \frac{e^{-sT_s}G_{\mathrm{BPF}}(s)G_{\mathrm{PR\_C}}(s)Y_{\mathrm{mad}}(s)}{W_{\mathrm{qmad}}(s)\left[(L_{\mathrm{q}}s+R_{\mathrm{s}})+e^{-1.5sTs}G_{\mathrm{q}}(s)\right]}. \tag{10}$$

Therefore, the small-signal variations of the rectified current can be expressed as

$$\Delta i_{\mathrm{L}}(s) = \frac{G_{\mathrm{L}}(s)}{1+G_{\mathrm{L}}(s)}\Delta i_{\mathrm{Lref}} + \frac{C_{\mathrm{dc}}s}{1+G_{\mathrm{L}}(s)}\Delta u_{\mathrm{dc}} + \frac{\left(1-e^{-1.5sT_{\mathrm{s}}}\right)U_{\mathrm{qref0}}Y_{\mathrm{mad}}(s)}{U_{\mathrm{dc0}}W_{\mathrm{qmad}}(s)\left(1+G_{\mathrm{L}}(s)\right)\left[(L_{\mathrm{q}}s+R_{\mathrm{s}})+e^{-0.5sT_s}G_{\mathrm{q}}(s)\right]}\Delta u_{\mathrm{dc}}. \tag{11}$$

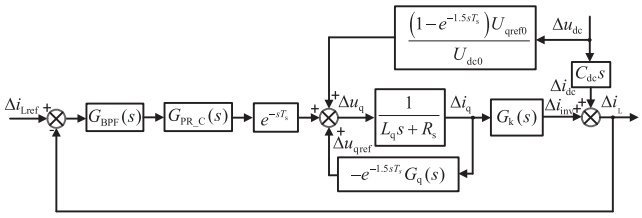

Fig. 3. Small-signal block diagram of RCR.

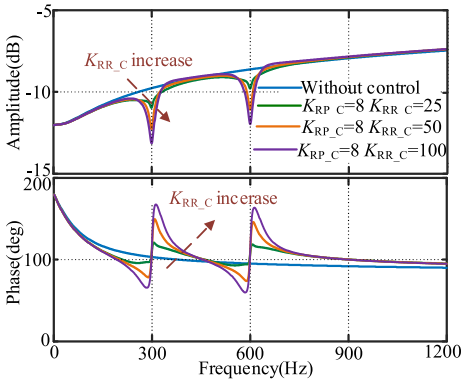

Fig. 4. Nyquist diagrams of $Y_{mad}(s)/Y_{LC}(s)$ under different resonant parameters. (a) Overall view. (b) Zoomed view.

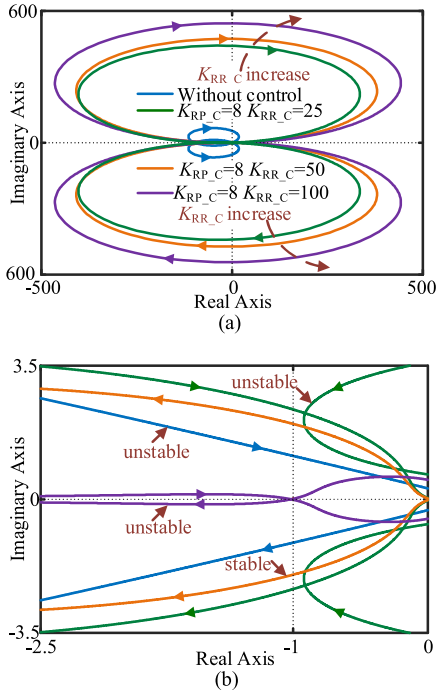

Fig. 5. Bode diagrams of the transfer function between Δi_L and Δu_d.

Through the small-signal block diagram of RCR, it can be known that the digital control delay and fluctuated dc-link voltage will introduce disturbances to RCR.

C. Analysis of Current Harmonics and Stability

From (11), the transfer function $G_D(s)$ between Δi_L and Δu_{dc} can be expressed as

$$G_D(s) = \frac{C_{dc}s}{1+G_L(s)} + \frac{(1-e^{-1.5sT_s})U_{qref0}Y_{mad}(s)}{U_{dc0}W_{qmad}(s)(1+G_L(s))\left[(L_q s+R)+e^{-0.5sT_s}G_q(s)\right]}. \tag{12}$$

The grid voltage in this study is 380 V/50 Hz. Based on steady-state operating point data obtained from offline tests of the experimental motor at rated power, the Bode diagrams of $G_D(s)$ under different parameters of the current proportion resonant controller is shown in Fig. 4. The amplitudes of $G_D(s)$ at 300 Hz (6th harmonic) and 600 Hz (12th harmonic) decrease as K_{RR_C} increases in a certain range, which indicates an enhanced suppression effect on the 300 and 600 Hz harmonics caused by the disturbances of the dc-link voltage.

Considering the electrolytic capacitorless PMSM as a cascade system that is composed of the output admittance of the grid side $Y_{LC}(s)$ and the input admittance of the inverter $Y_{mad}(s)$, the stability of the drive can be analyzed by the Nyquist diagram of the admittance ratio $Y_{mad}(s)/Y_{LC}(s)$. The $Y_{LC}(s)$ can be denoted as

$$Y_{LC}(s) = \frac{L_g C_{dc}s^2 + R_g C_{dc}s + 1}{L_g s + R_g} \tag{13}$$

where R_g is the line resistance and L_g is the grid inductance.

Under different K_{RR_C}, the Nyquist diagram of the admittance ratio $Y_{mad}(s)/Y_{LC}(s)$ is shown in Fig. 5. When RCR is not applied, the system is unstable due to the reduction of the dc-link capacitance. Within a certain range, the intersection of the Nyquist diagram with the negative real axis shifts from the left of (–1, *j*0) toward the point (–1, *j*0) as K_{RR_C} increases, which means the stability of the system is improved. When $K_{RP\_C} = 8$ and $K_{RR\_C} = 50$, the intersection is at the right of (–1, *j*0), and the system is stable. However, if K_{RR_C} is increased to 100, the intersection moves to the left of (–1, *j*0), and the system tends to be unstable.

Based on Fig. 4, it can be seen that when $K_{RP\_C} = 8$ and $K_{RR\_C} = 50$, the magnitudes of $G_D(s)$ at 300 and 600 Hz are –12.2 and –11.1 dB, respectively. The RCR has limited effectiveness in suppressing the disturbances caused by the digital control delay and fluctuated dc-link voltage. Increasing

$$Y_{mad}(s) = \frac{2U_{dc0}Y_{mi}(s)+3G_{mad}(s)A_{1q}(s)C_{dc}s\left(U_{d0}+\omega_e L_d I_{q0}+L_d I_{d0}s+I_{d0}R_s\right)-3G_{mad}(s)A_{1d}(s)C_{dc}s\left(U_{q0}-\omega_e L_q I_{d0}+L_q I_{q0}s+I_{q0}R_s\right)}{2U_{dc0}-3G_{mad}(s)A_{1q}(s)\left(U_{d0}+\omega_e L_d I_{q0}+L_d I_{d0}s+I_{d0}R_s\right)+3G_{mad}(s)A_{1d}(s)\left(U_{q0}-\omega_e L_q I_{d0}+L_q I_{q0}s+I_{q0}R_s\right)} \tag{7}$$

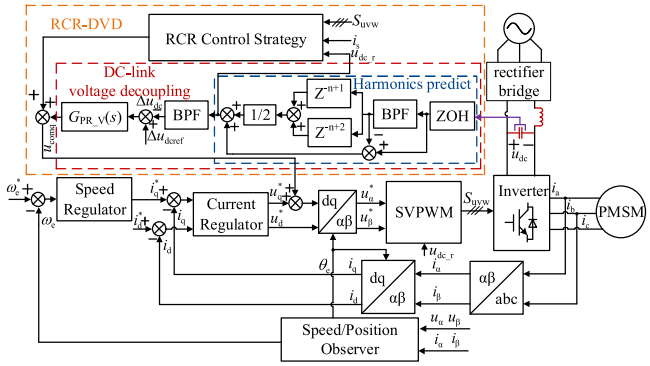

Fig. 6. Control block diagram of the proposed RCR-DVD.

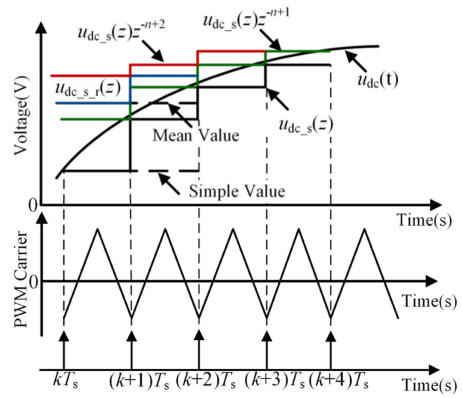

Fig. 7. Schematic diagram for prediction of DC-link voltage harmonics.

the resonant coefficient of the controller can further suppress the disturbances, but the system becomes unstable gradually.

Therefore, it is necessary to improve RCR to reduce the negative impact of the disturbances on the harmonic suppression and system stability.

III. Proposed Harmonic Suppression Method Based on RCR With DC-Link Voltage Decoupling

A. Scheme of the Proposed Harmonic Suppression Method

According to (11), the disturbances in RCR are mainly introduced by the digital control delay, as well as the energy storage effect of the dc-link capacitors. Based on RCR, the sampled dc-link voltage is decoupled to compensate the disturbances. Utilizing the periodical characteristic of the harmonics in dc-link voltage, the main harmonics are predicted to compensate the digital control delay. A closed-loop control for main harmonics in the dc-link voltage is constructed to suppress the voltage disturbances in RCR and further improve the quality of grid currents. The rotor position θ_e is obtained through the sensorless observers [31], [32]. The overall control block diagram is shown in Fig. 6.

Fig. 7 shows the diagram for predicting the harmonic components of the dc-link voltage. The harmonics of dc-link voltage sampled at nT_s can be expressed as

$$u_{dc\_s}(z) = u_{dc\_e} G_{BPF}(z) \tag{14}$$

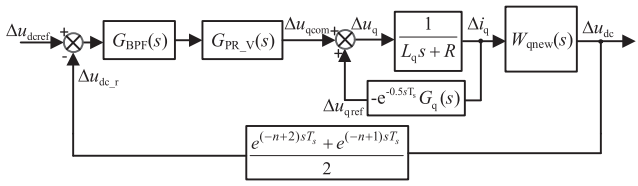

Fig. 8. Block diagram of DC-link voltage decoupling.

where u_{dc_e} is the equivalent sampled dc-link voltage, and $G_{BPF}(z)$ is the discrete form of bandpass filter transfer function.

The harmonics of dc-link voltage sampled at nT_s participate in the nth duty cycle signal updating. At $(n+1)T_s$, the duty cycle of the nT_s moment is outputted. If the average values of the harmonics in dc-link voltage at $(n+1)T_s$ and $(n+2)T_s$ can be obtained at nT_s, the digital control delay of the dc-link voltage harmonics can be effectively reduced. Utilizing the periodic characteristics of the dc-link voltage, the sampled values of the dc-link voltage harmonics that are one or two sampling periods ahead can be represented as $u_{dc\_s}(z)z^{-n+1}$ and $u_{dc\_s}(z)z^{-n+2}$, respectively. Therefore, the average values of the dc-link voltage harmonics at $(n+1)T_s$ and $(n+2)T_s$ can be approximately represented as

$$u_{dc\_s\_r}(z) = \frac{\left(u_{dc\_s}(z)z^{-n+2} + u_{dc\_s}(z)z^{-n+1}\right)}{2} \tag{15}$$

$$n = \frac{k f_s}{N f_g} \tag{16}$$

where $u_{dc\_s\_r}(z)$ represents the predicted harmonics component of the dc-link voltage, f_s is the switching frequency, k is the rounding coefficient, and N is the harmonic order.

Therefore, the predicted dc-link voltage can be expressed as

$$u_{dc\_r} = u_{dc} - u_{dc\_s} + u_{dc\_s\_r}. \tag{17}$$

B. DC-Link Voltage Decoupling Strategy

In order to suppress the disturbance caused by the fluctuated dc-link voltage, the dc-link voltage decoupling strategy is proposed. The small-signal block diagram of dc-link voltage decoupling strategy is shown in Fig. 8. As can be seen, the small-signal variations of the predicted dc-link voltage are obtained as feedback, and the difference between the reference dc-link voltage and the predicted dc-link voltage is inputted to the voltage proportional resonance controller. The compensation signal of the q-axis voltage is obtained through the controller and added to the reference voltage at q axes.

After applying the RCR-DVD control strategy, $\Delta u_{d,qref}$ can be expressed as

$$\begin{bmatrix}\Delta u_{dref}(s)\\ \Delta u_{qref}(s)\end{bmatrix} = \begin{bmatrix}-G_d(s) & -\omega_e L_q\\ \omega_e L_d & -G_q(s)\end{bmatrix}\begin{bmatrix}\Delta i_d(s)\\ \Delta i_q(s)\end{bmatrix} + \begin{bmatrix}0\\ -G_{BPF}(s)G_{PR\_C}(s)\Delta i_{L\_r}(s)\end{bmatrix} + \begin{bmatrix}0\\ -G_{BPF}(s)G_{PR\_V}(s)\Delta u_{dc}(s)\end{bmatrix} \tag{18}$$

where $G_{PR\_V}(s)$ is the transfer function of the voltage proportional resonant controller.

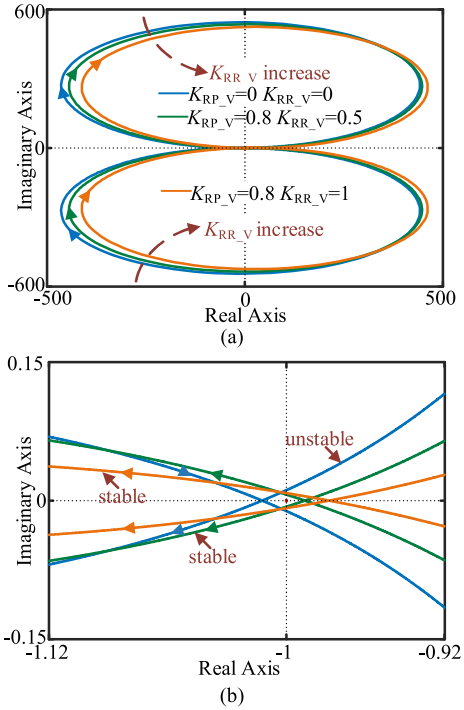

Fig. 9. Nyquist diagrams of $Y_{\rm new}(s)/Y_{\rm LC}(s)$ under different resonant parameters. (a) Overall view. (b) Zoomed view.

Combining the voltage in *dq* axes, the transfer function between $\Delta i_{\rm dq}$ and $\Delta u_{\rm dc}$ after applying the RCR-DVD can be expressed as

$$\begin{bmatrix} W_{\rm qnew}(s) \\ W_{\rm qnew}(s) \end{bmatrix} = \frac{1}{\Delta u_{\rm dc}} \begin{bmatrix} \Delta i_{\rm d}(s) \\ \Delta i_{\rm q}(s) \end{bmatrix} = \begin{bmatrix} W_{\rm d}(s) \\ W_{\rm q}(s) \end{bmatrix} + G_{\rm mad}(s) \frac{\Delta i_{\rm L}(s)}{\Delta u_{\rm dc}(s)} \begin{bmatrix} A_{1\rm q}(s) \\ -A_{1\rm d}(s) \end{bmatrix} + G_{\rm mad2}(s) \begin{bmatrix} A_{1\rm q}(s) \\ -A_{1\rm d}(s) \end{bmatrix} \tag{19}$$

where $G_{\rm mad2}(s)$ can be expressed as

$$G_{\rm mad2}(s) = \frac{-G_{\rm BPF}(s) G_{\rm PR\_V}(s)}{A_{2\rm q}(s) A_{1\rm d}(s) - A_{2\rm d}(s) A_{1\rm q}(s)}. \tag{20}$$

Therefore, the input impedance of the motor drive $Y_{\rm new}(s)$ after applying the proposed strategy can be expressed as (21) shown at the bottom of the next page. Through the small-signal model, it can be known that the input admittance of the inverter is changed with RCR-DVD, which improves the harmonics suppression ability and stability of the system.

As analyzed in Fig. 4, when $K_{\rm RP\_C} = 8$ and $K_{\rm RR\_C} = 100$, applying only RCR can improve the harmonics suppression capability of the disturbances, but the system becomes unstable. The Nyquist diagram of $Y_{\rm new}(s)/Y_{\rm LC}(s)$ after applying RCR-DVD is shown in Fig. 9. It can be seen that the intersection shifts from the left of the (–1, *j*0) axis to the right, and the control system becomes stable under the same parameters of the current proportional resonant controller.

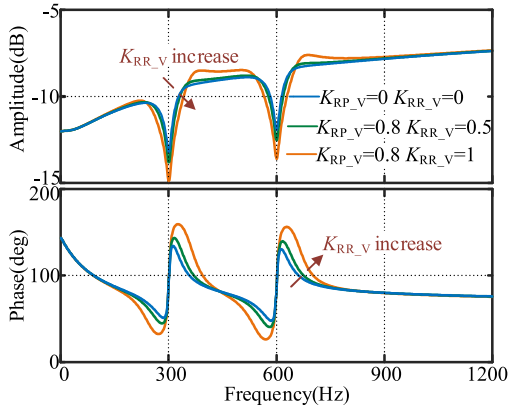

Fig. 10. Bode diagrams of the transfer function between $\Delta i_{\rm L}$ and $\Delta u_{\rm d}$.

C. Analysis of Harmonic Suppression Capability

Fig. 10 shows the Bode diagram of $G_{\rm D}(s)$ after applying RCR-DVD. The amplitude of $G_{\rm D}(s)$ decreases at 300 and 600 Hz with the appliance of the proposed strategy, which means harmonics suppression performance is enhanced.

As shown in Fig. 9, after applying the proposed control strategy, the stability of the control system is improved. Therefore, applying RCR-DVD can not only enhance the ability of RCR on harmonics suppression but also improve the stability of the system.

After applying RCR-DVD, the transfer function $G_{\rm y}(s)$ between $\Delta u_{\rm dc}$ and the rectified voltage $\Delta u_{\rm grec}$ can be expressed as

$$G_{\rm y}(s) = \frac{1}{(L_{\rm g}s + R_{\rm g})\left[sC_{\rm dc} + Y_{\rm new}(s)\right] + 1}. \tag{22}$$

The grid-side input impedance $Z_{\rm gmad}$(s) can be expressed as

$$Z_{\rm gmad}(s) = R_{\rm g} + sL_{\rm g} + \frac{1}{C_{\rm dc}s + Y_{\rm new}(s)}. \tag{23}$$

The Bode diagram of $G_{\rm y}$(s) before and after applying the control strategies is shown in Fig. 11. Without control, a resonance peak occurs, which results in the amplification of harmonics in the dc-link voltage. The resonance peak can be reduced slightly after applying only RCR. Furthermore, after applying the proposed control strategy, the resonance peak is further reduced, which means the dc-link voltage harmonics can be further suppressed.

The Bode diagram of the grid side input impedance $Z_{\rm gmad}(s)$ before and after applying the control strategies is shown in Fig. 12. Without control, the input impedance at the resonance frequency is relatively small, which leads to significant harmonics in the rectified current. After applying RCR, the amplitude of the input impedance at the resonance frequency increases. Further applying the proposed strategy, the amplitude of impedance at 300 and 600 Hz increases, which effectively suppresses the harmonics of grid currents at these frequencies.

IV. Experimental Results

The proposed control strategy is verified on a 5.5 kW experimental platform. Fig. 13 shows the experimental platform of the

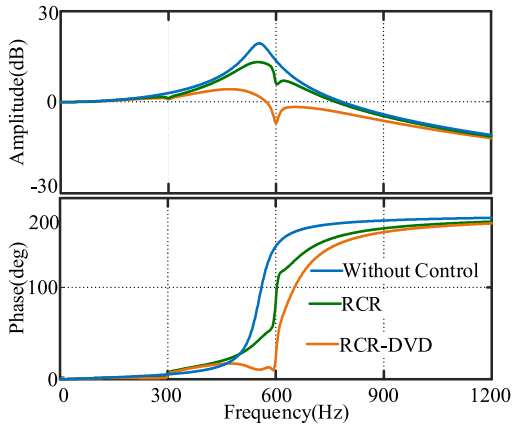

Fig. 11. Bode diagram of the transfer function between the DC-link voltage and the rectified voltage.

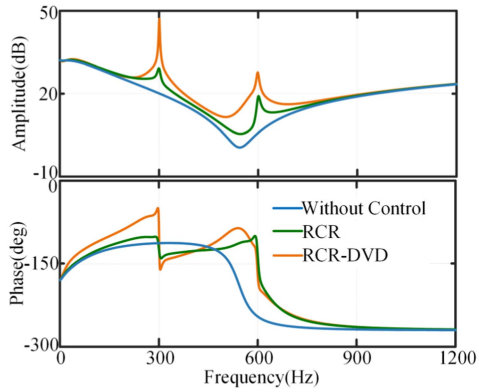

Fig. 12. Bode diagram of the grid-side input impedance before and after applying the control strategies.

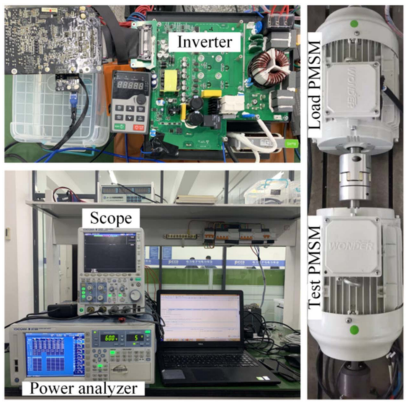

Fig. 13. Experimental platform for electrolytic capacitorless PMSM drive.

TABLE I
PARAMETERS OF THE EXPERIMENTAL PLATFORM

Parameters	Value
Capacitance (μF)	30
Inductance (mH)	2.5
q-axis inductance (mH)	17.2
d-axis inductance (mH)	7.5
Stator resistance (Ω)	0.265
Rated frequency (Hz)	75

electrolytic capacitorless PMSM drive. The dc-link capacitance is chosen as 30 μF by taking into account the quality of grid currents and stability of the system. The control algorithm is implemented in a DSP28075 chip, with the switching frequency and sampling frequency of 8 kHz, which is commonly used in HVAC application. Another motor of the same model operates in generation mode to provide a load torque. In the platform, a voltage sensor is applied for dc-link voltage detection, which is a common solution in motor drives for safety and operation performance improvement. The main parameters of the experimental platform are shown in Table I.

Fig. 14(a) shows the experiment results of the harmonics at 300 and 600 Hz in the dc-link voltage before and after applying the control strategies at the motor frequency of 75 Hz. As shown in Fig. 14(b), the amplitudes of the harmonics voltages at 300 and 600 Hz before applying the control are 49.9 and 15.3 V, respectively. After applying RCR, the amplitudes of the corresponding harmonics are decreased to 39.8 and 11.2 V, respectively, which is shown in Fig. 14(c). With the harmonics prediction, the amplitudes of the corresponding harmonics decrease to 37.9 and 6.13 V, as shown in Fig. 14(d). Fig. 14(e) shows that after applying RCR-DVD, the amplitudes of the corresponding harmonic are further decreased to 32.6 and 4.6 V. The results indicate that applying RCR-DVD can significantly reduce the amplitudes of harmonics in dc-link voltage compared to RCR.

Fig. 15(a) shows harmonics at 300 and 600 Hz in the rectified current before and after applying the control strategies. As shown in Fig. 15(b), the amplitudes of harmonics at 300 and 600 Hz in the rectified current before applying the control are 2.6 and 1.7 A, respectively. After applying RCR, the amplitudes of the corresponding harmonics decrease to 0.4 and 1.4 A, which is shown in Fig. 15(c). With the harmonics prediction, the amplitudes of the corresponding harmonics decrease to 0.5 and 1 A, as shown in Fig. 15(d). Fig. 15(e) shows that after applying RCR-DVD, the amplitudes of corresponding harmonics can be further decreased to 0.05 and 0.5 A.

Fig. 16 shows the waveforms of the u-phase grid current and dc-link voltage before and after applying the control strategies. The waveforms of the dc-link voltage and grid current before and

$$Y_{\text{new}}(s) = \frac{\begin{array}{c}2U_{\text{dc0}}Y_{\text{mi}}(s)+3\left(G_{\text{mad}}A_{1\text{q}}(s)C_{\text{dc}}s+G_{\text{mad2}}A_{1\text{q}}(s)\right)\left(U_{\text{d0}}+\omega_{\text{e}}L_{\text{d}}I_{\text{q0}}+L_{\text{d}}I_{\text{d0}}s+I_{\text{d0}}R_{\text{s}}\right)\\ -3\left(G_{\text{mad}}A_{1\text{d}}(s)C_{\text{dc}}s+G_{\text{mad2}}A_{1\text{d}}(s)\right)\left(U_{\text{q0}}-\omega_{\text{e}}L_{\text{q}}I_{\text{d0}}+L_{\text{q}}I_{\text{q0}}s+I_{\text{q0}}R_{\text{s}}\right)\end{array}}{2U_{\text{dc0}}-3G_{\text{mad}}A_{1\text{q}}(s)\left(U_{\text{d0}}+\omega_{\text{e}}L_{\text{d}}I_{\text{q0}}+L_{\text{d}}I_{\text{d0}}s+I_{\text{d0}}R_{\text{s}}\right)+3G_{\text{mad}}A_{1\text{d}}(s)\left(U_{\text{q0}}-\omega_{\text{e}}L_{\text{q}}I_{\text{d0}}+L_{\text{q}}I_{\text{q0}}s+I_{\text{q0}}R_{\text{s}}\right)}. \quad (21)$$

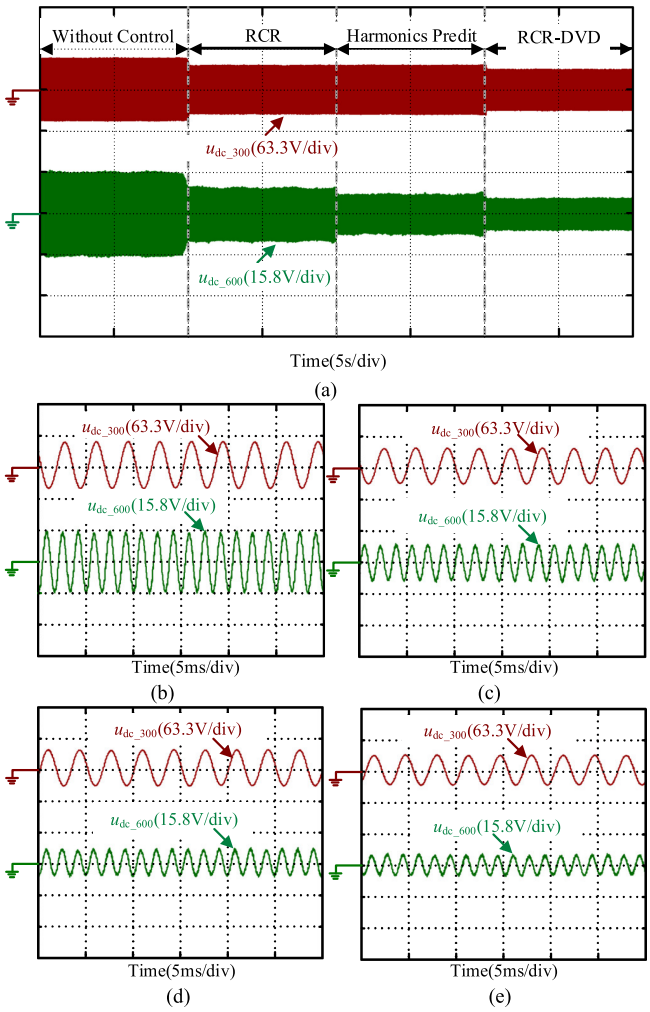

Fig. 14. Experimental results of DC-link voltage harmonic suppression. (a) Enable control strategies. (b) Zoomed view without control. (c) Zoomed view with RCR. (d) Zoomed view with main harmonics prediction. (e) Zoomed view with RCR-DVD.

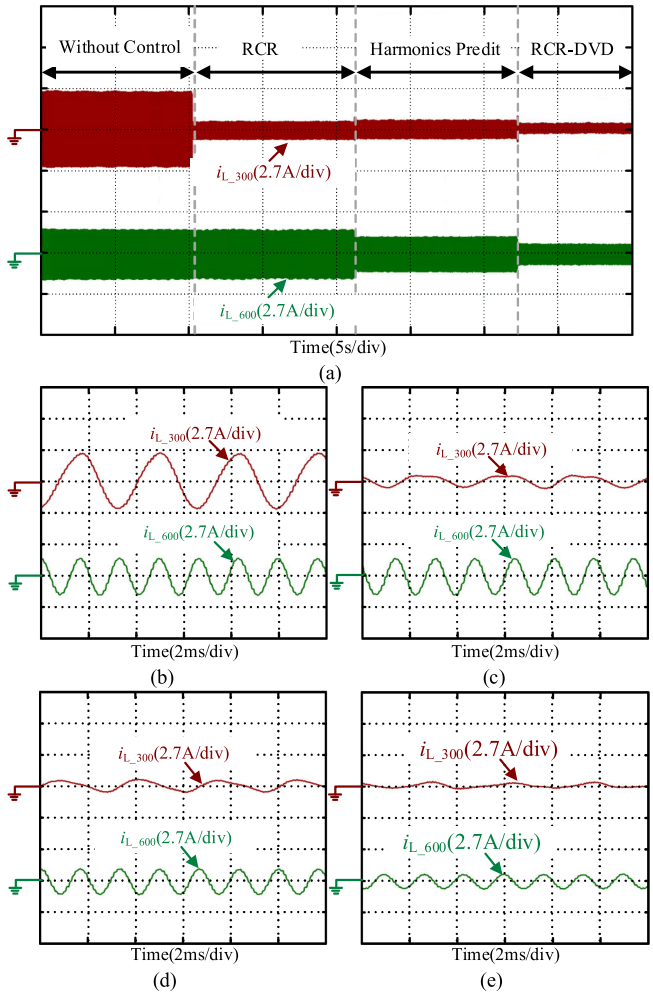

Fig. 15. Experimental results of inductive current harmonic suppression. (a) Enable control strategies. (b) Zoomed view without control. (c) Zoomed view with RCR. (d) Zoomed view with main harmonics prediction. (e) Zoomed view with RCR-DVD.

after applying RCR are shown in Fig. 16(b) and (c), respectively. After applying RCR, the THD of grid current decreases from 45.6% to 33.8%, and fluctuation of the dc-link voltage decreases from 145.7 to 107.9 V. With the harmonics prediction, the THD of grid currents decreases to 32.9%, and fluctuation of the dc-link voltage decreases from 107.9 to 81.1 V, as shown in Fig. 16(d). Fig. 16(e) shows the waveforms after applying RCR-DVD. The suppression effect on the grid current and dc-link voltage harmonics is further improved. The THD of the grid current is further decreased to 30.6% and the fluctuation of dc-link voltage decreases to 66.1 V. Fourier analysis shows that compared with the waveform before the control, the 5th, 11th, and 13th harmonics component in the grid current are reduced after applying RCR. With the proposed strategy, the 7th, 11th, and 13th harmonics components in the grid current are further reduced. After applying RCR-DVD, the fluctuation of the dc-link voltage vector and the THD of the gird current are significantly decreased, resulting in an improvement in the quality of grid currents.

Fig. 17 shows the experimental results of the grid current at the motor speed of 75 Hz with RCR-DVD under the condition that the load torque of the motor steps from 25 to 50 N·m and back to 25 N·m. It can be known that the THD of the grid current is decreased from 34% to 31% when the load torque steps from 25 to 50 N·m. The proposed control strategy can effectively improve the quality of the grid current under the load step condition.

Fig. 18 shows the experimental results with RCR-DVD when the motor speed varies from 45 to 75 Hz and back to 45 Hz. The load torques of the motor are 30 and 50 N·m when the motor speeds are 45 and 75 Hz, respectively. It can be seen from the region of motor speed at 75 Hz that the fluctuation of the dc-link voltage increases from 65 to 72 V, and the torque ripple increases from 8.2 to 8.4 N·m. The THD of the grid current decreases from 34% to 31% as the speed of the motor increases. The result shows that the proposed control method can effectively improve the quality of the grid current when the speed changes.

Fig. 19 shows the experimental results of the q-axis current, dc-link voltage, motor current, and the grid current under motor frequency of 75 Hz. Fig. 19(a) shows the Fourier analysis of the

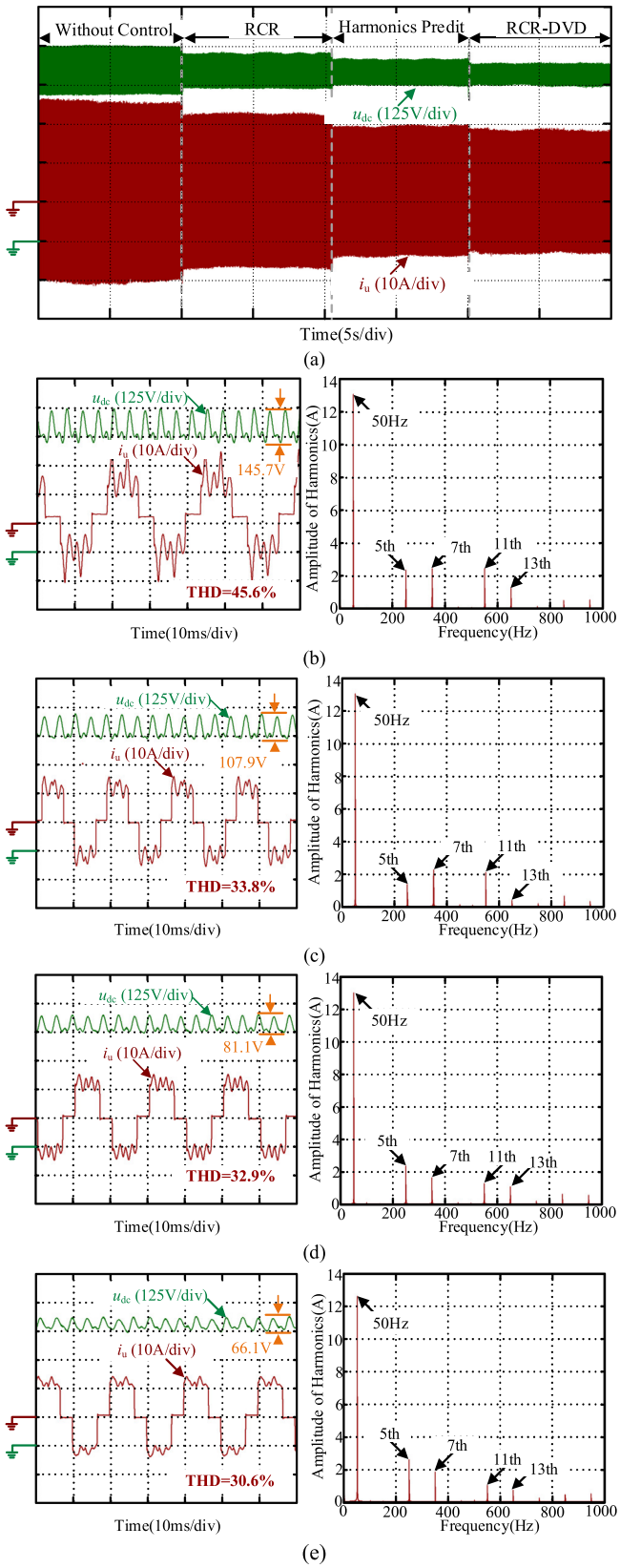

Fig. 16. Experimental results of DC-link voltage and grid current. (a) Enable control strategies. (b) Zoomed view without control and Fourier analysis of the grid current. (c) Zoomed view with RCR and Fourier analysis of the grid current. (d) Zoomed view with main harmonics prediction and Fourier analysis of the grid current. (e) Zoomed view with RCR-DVD and Fourier analysis of the grid current.

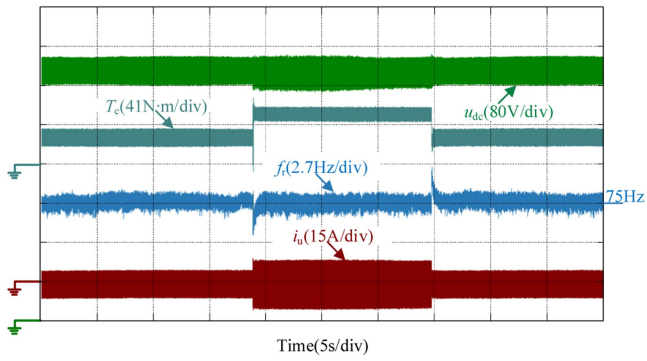

Fig. 17. Experimental results of the load step.

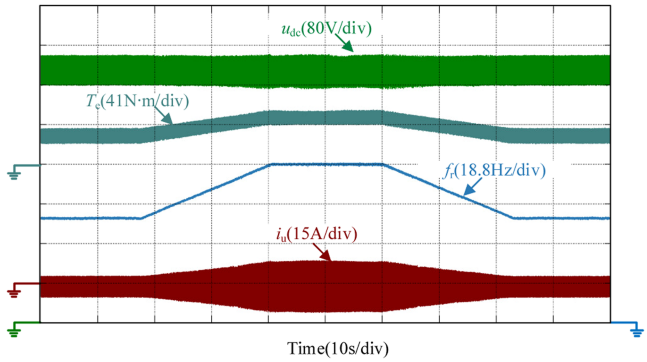

Fig. 18. Experimental results of the speed dynamic process.

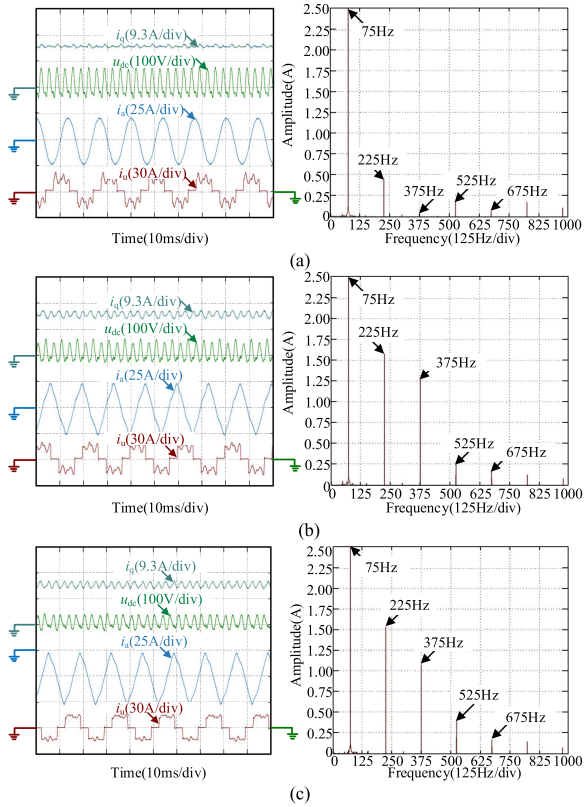

Fig. 19. Experimental results of the motor current under the motor frequency of 75 Hz. (a) Waveform without control and Fourier analysis of the motor current. (b) Waveform with RCR and Fourier analysis of the motor current. (c) Waveform view with RCR-DVD and Fourier analysis of the motor current.

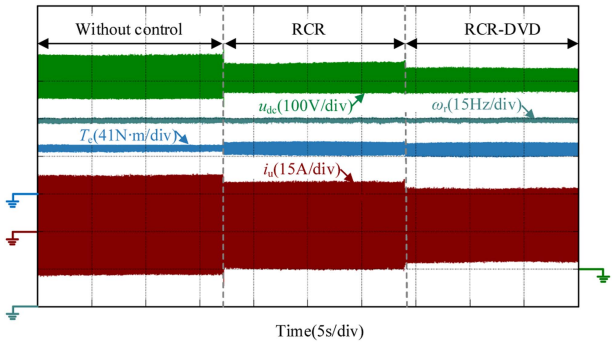

Fig. 20. Experimental result of the motor torque under the motor frequency of 75 Hz.

motor current without control. The amplitudes of the harmonics at 225, 375, 525, and 675 Hz in the motor current are 0.47, 0.04, 0.16, and 0.07 A, respectively. After applying the RCR, the amplitudes of the corresponding harmonics are 1.60, 1.28, 0.25, and 0.18 A, respectively, as shown in Fig. 19(b). By applying the RCR-DVD, the amplitudes of the harmonics are 1.52, 1.07, 0.41, and 0.17 A, respectively, as shown in Fig. 19(c). As can be seen, applying conventional RCR and proposed RCR-DVD will increase the harmonics in motor current. However, compared with RCR, the harmonics in the motor current can be reduced using RCR-DVD.

Fig. 20 shows the experimental results of the dc-link voltage, angular frequency of the motor, motor torque, and the grid current under the motor speed of 75 Hz. It can be seen that the torque ripple increases from 4.6 to 8.4 N·m after applying RCR. By applying the RCR-DVD, the torque ripple decreases to 7.9 N·m. The fluctuation amplitude of the motor speed increases from 0.72 to 0.82 Hz after applying the RCR. By applying the RCR-DVD, the fluctuation amplitude of the motor speed decreases to 0.75 Hz. It can be known that compared with only applying the RCR, the proposed control strategy can decrease the torque ripple.

Fig. 21(a) shows experimental results when the grid voltage contains 5th harmonics under the motor speed of 75 Hz. After applying the RCR, the amplitudes of the harmonics at 300 and 600 Hz in the rectified current decrease from 2.2 and 1.1 A to 1.1 0.9 A, respectively. After applying the RCR-DVD, the amplitudes of the corresponding harmonics further decrease to 0.9 and 0.7 A, respectively. The magnitude of the dc-link voltage fluctuation decreases from 173 to 167 V after applying RCR. By applying the RCR-DVD, the magnitude of the dc-link voltage fluctuation decreases to 152 V. Fig. 21(b) shows experimental results when the grid voltage contains 7th harmonics under the motor speed of 75 Hz. After applying the RCR, the amplitudes of the harmonics at 300 and 600 Hz in the rectified current decrease from 2.5 and 1.2 A to 1.3 and 0.9 A, respectively. After applying the RCR-DVD, the amplitudes of the harmonics decrease to 1.1 and 0.8 A, respectively. The magnitude of the dc-link voltage fluctuation decreases from 162 to 158 V after applying RCR. By applying the RCR-DVD, the magnitude of the dc-link voltage fluctuation decreases to 129 V. It can be known that the proposed strategy can still work when the grid voltage contains unknown harmonics like 5th and 7th order.

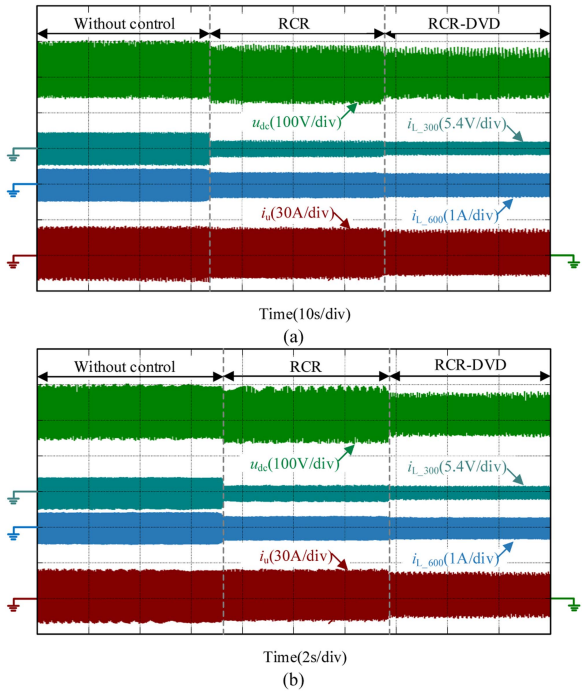

Fig. 21. Experimental results of the grid current under the condition that grid voltage contains 5th and 7th harmonics. (a) Grid voltage contains 5th harmonic. (b) Grid voltage contains 7th harmonic.

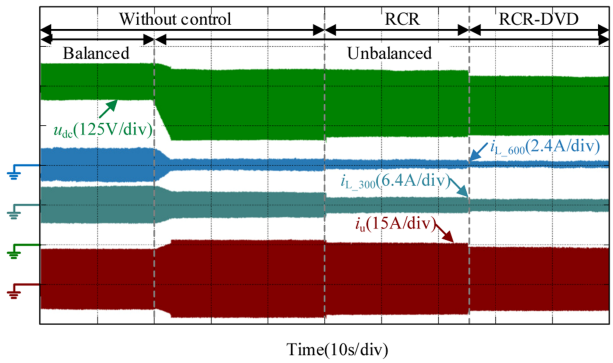

Fig. 22. Experimental results under the balanced and unbalanced grid condition.

Fig. 22 shows the experimental results of the dc-link voltage, the harmonic at 300 and 600 Hz in rectified current, and u-phase input current of the grid side under unsymmetrical grid voltages at the motor frequency of 50 Hz. In order to simulate the unsymmetrical grid voltages, the amplitude of u-phase input voltage is dropped by 30%. The phase differences with the v-phase and w-phase voltages are 125° and 245°, respectively. As can be seen, the amplitudes of harmonics at 300 and 600 Hz in the rectified current decrease from 2.6 and 0.9 A to 1.8 and 0.4 A, respectively, and the THD of the grid current increases from 59.57% to 71.36% when the input grid voltage turns into unbalanced. After applying the RCR, the amplitudes of corresponding harmonics in the rectified current decrease from 1.8 and 0.4 A to 1.1 and 0.2 A, respectively. The THD the of grid current decreases to 65.38%. After applying the RCR-DVD, the amplitudes of corresponding harmonics decrease from 1.1 and

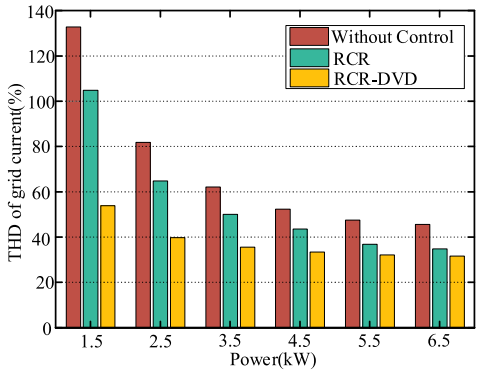

Fig. 23. THD of grid-side current before and after applying control strategies at different power levels.

0.2 A to 0.7 and 0.1 A, respectively. The THD the of grid current decreases to 60.68%.

Fig. 23 shows the THD of the grid current after applying RCR-DVD at different power levels. As can be seen, when the motor out power is low, the control effects of RCR-DVD are evident. When the motor is operating at high power level, the additional control effects may not be evident from the perspective of THD, due to the larger fundamental current.

V. Conclusion

In this article, a grid currents harmonics suppression strategy based on the RCR-DVD is proposed. The disturbances, which are the side effect on the rectified current control, caused by the fluctuated dc-link voltage and digital control delay in RCR are revealed by the established small-signal model of the system. A dc-link voltage decoupling method is proposed to predict the main harmonics in dc-link voltage and construct a closed-loop feedback control. After applying the proposed strategy, the input impedance of the grid side can be significantly increased, which means the proposed method can reduce the influence of the disturbances branch on RCR, and enhance the rectified current control. The experimental results show that the proposed method can reduce the harmonics both in grid current and dc-link voltage. Specifically, THD of the grid currents can be reduced to 30.6%, which is close to the theoretical minimum value of 29.7%. The dc-link voltage fluctuation can be reduced to 45.4%.

Appendix

From (3), combining with the voltages in dq axes, the relationship between $\Delta i_{\mathrm{d,q}}$ and Δu_{dc} can be expressed as

$$\begin{bmatrix}\mathbf{A}_{1\mathrm{d}}(s) & \mathbf{A}_{1\mathrm{q}}(s)\\ \mathbf{A}_{2\mathrm{d}}(s) & \mathbf{A}_{2\mathrm{q}}(s)\end{bmatrix}\begin{bmatrix}\Delta i_{\mathrm{d}}\\ \Delta i_{\mathrm{q}}\end{bmatrix}=\frac{\left(1-e^{-1.5sT_{\mathrm{s}}}\right)\Delta u_{\mathrm{dc}}}{U_{\mathrm{dc0}}}\begin{bmatrix}U_{\mathrm{dref0}}\\ U_{\mathrm{qref0}}\end{bmatrix}+e^{-sT_{\mathrm{s}}}\begin{bmatrix}0\\ -G_{\mathrm{BPF}}(s)G_{\mathrm{PR\_C}}(s)\Delta i_{\mathrm{L\_r}}(s)\end{bmatrix}\tag{A1}$$

where $A_{1\mathrm{d,q}}(s)$ and $A_{2\mathrm{d,q}}(s)$ can be expressed as follows:

$$\begin{bmatrix}A_{1\mathrm{d}}(s) & A_{1\mathrm{q}}(s)\\ A_{2\mathrm{d}}(s) & A_{2\mathrm{q}}(s)\end{bmatrix}=\begin{bmatrix}R_{\mathrm{s}}+sL_{\mathrm{d}} & -\omega_{\mathrm{e}}L_{\mathrm{q}}\\ \omega_{\mathrm{e}}L_{\mathrm{d}} & R_{\mathrm{s}}+sL_{\mathrm{q}}\end{bmatrix}+e^{-1.5sT_{\mathrm{s}}}\begin{bmatrix}G_{\mathrm{d}}(s) & \omega_{\mathrm{e}}L_{\mathrm{q}}\\ -\omega_{\mathrm{e}}L_{\mathrm{d}} & G_{\mathrm{q}}(s)\end{bmatrix}.\tag{A2}$$

$W_{\mathrm{d,q}}(s)$ is the transfer function between $\Delta i_{\mathrm{d,q}}$ and Δu_{dc} when the control is not applied

$$\begin{bmatrix}W_{\mathrm{d}}(s)\\ W_{\mathrm{q}}(s)\end{bmatrix}=\frac{\left(1-e^{-1.5sT_{\mathrm{s}}}\right)}{U_{\mathrm{dc0}}\left[A_{2\mathrm{q}}(s)A_{1\mathrm{d}}(s)-A_{2\mathrm{d}}(s)A_{1\mathrm{q}}(s)\right]}\cdot\begin{bmatrix}U_{\mathrm{dref0}}A_{2\mathrm{q}}(s)-U_{\mathrm{qref0}}A_{1\mathrm{q}}(s)\\ U_{\mathrm{qref0}}A_{1\mathrm{d}}(s)-U_{\mathrm{dref0}}A_{2\mathrm{d}}(s)\end{bmatrix}.\tag{A3}$$

$G_{\mathrm{mad}}(s)$ is the simplified expression of the gain coefficient caused by RCR

$$G_{\mathrm{mad}}(s)=\frac{e^{-sT_{\mathrm{s}}}G_{\mathrm{PR\_C}}(s)G_{\mathrm{BPF}}(s)}{A_{2\mathrm{q}}(s)A_{1\mathrm{d}}(s)-A_{2\mathrm{d}}(s)A_{1\mathrm{q}}(s)}.\tag{A4}$$

References

[1] M. Esteki, D. Darvishrahimabadi, M. Shahabbasi, and S. A. Khajehoddin, "An electrolytic-capacitor-less PFC LED driver with low DC-bus voltage stress for high power streetlighting applications," *IEEE Trans. Power Electron.*, vol. 38, no. 5, pp. 6294–6310, May 2023.

[2] H. Kim, J. Park, S. Kim, R. M. Hakim, H. Belkamel, and S. Choi, "A single-stage electrolytic capacitor-less EV charger with single- and three-phase compatibility," *IEEE Trans. Power Electron.*, vol. 37, no. 6, pp. 6780–6791, Jun. 2022.

[3] D. Bao, Y. Wang, and X. Pan, "Integrate-power-control-strategy-based electrolytic capacitor-less back-to-back converter for variable frequency speed control system," in *Proc. IEEE Int. Power Electron. Appl. Conf. Expo.*, Nov. 2018, pp. 1–5.

[4] G. Wang, M. Valla, and J. Solsona, "Position sensorless permanent magnet synchronous machine drives—A review," *IEEE Trans. Ind. Electron.*, vol. 67, no. 7, pp. 5830–5842, Jul. 2020.

[5] Y. Ohno and H. Haga, "Control method of electrolytic capacitorless dual inverter for harmonic compensation under distorted grid voltage," *IEEE Trans. Ind. Appl.*, vol. 58, no. 1, pp. 375–387, Jan./Feb. 2022.

[6] B. Zheng, Y. Cao, X. Li, and T. Shi, "An improved DC-link series IGBT chopping strategy for brushless DC motor drive with small DC-link capacitance," *IEEE Trans. Energy Convers.*, vol. 36, no. 1, pp. 242–252, Mar. 2021.

[7] Y. Son and J. I. Ha, "Discontinuous grid current control of motor drive system with single-phase diode rectifier and small DC-link capacitor," *IEEE Trans. Power Electron.*, vol. 32, no. 2, pp. 1324–1334, Feb. 2017.

[8] Y. Zhou, W. Huang, and F. Hong, "Single-phase input variable-speed AC motor system based on an electrolytic capacitor-less single-stage boost three phase inverter," *IEEE Trans. Power Electron.*, vol. 31, no. 10, pp. 7043–7052, Oct. 2016.

[9] C. Zhang, H. Xu, and X. Zhu, "A novel control strategy for electrolytic capacitor-less PMSM drive system," in *Proc. 20th Annu. IEEE Int. Conf. Elect. Mach. Syst.*, Aug. 2017, pp. 1–6.

[10] Y. Ohnuma and J. I. Itoh, "Comparison of boost chopper and active buffer as single to three phase converter," in *Proc. IEEE Energy Convers. Congr. Expo.*, Sep. 2011, pp. 515–521.

[11] W. Chen, Y. Zhang, Y. Tu, K. Shen, and J. Liu, "Active damping control for LCL filters with inverter-side current feedback only," *IEEE Trans. Power Electron.*, vol. 37, no. 9, pp. 10065–10069, Sep. 2022.

[12] H. Zhang, X. Wang, Y. He, D. Pan, and X. Ruan, "A compensation method to eliminate the impact of time delay on capacitor-current active damping," *IEEE Trans. Ind. Electron.*, vol. 69, no. 7, pp. 7512–7516, Jul. 2022.

[13] E. Rodriguez-Diaz, F. D. Freijedo, J. C. Vasquez, and J. M. Guerrero, "Analysis and comparison of notch filter and capacitor voltage feedforward active damping techniques for LCL grid-connected converters," *IEEE Trans. Power Electron.*, vol. 34, no. 4, pp. 3958–3972, Apr. 2019.

[14] W. J. Lee and S. K. Sul, "DC-link voltage stabilization for reduced DC-link capacitor inverter," *IEEE Trans. Ind. Appl.*, vol. 50, no. 1, pp. 404–414, Jan./Feb. 2014.

[15] N. Zhao, G. Wang, R. Zhang, B. Li, Y. Bai, and D. Xu, "Inductor current feedback active damping method for reduced DC-link capacitance IPMSM drives," *IEEE Trans. Power Electron.*, vol. 34, no. 5, pp. 4558–4568, May 2019.

[16] X. Liu, A. J. Forsyth, and A. M. Cross, "Negative input-resistance compensator for a constant power load," *IEEE Trans. Ind. Electron.*, vol. 53, no. 6, pp. 3188–3196, Dec. 2007.

[17] Y. Liu et al., "An active dc-link stabilization strategy for permanent magnet synchronous motor drive system based on inverter voltage compensation," *IEEE/ASME Trans. Mechatronics*, vol. 27, no. 5, pp. 2786–2795, Oct. 2022.
[18] Y. A.-R. I. Mohamed, A. A. A. Radwan, and T. K. Lee, "Decoupled reference-voltage-based active DC-link stabilization for PMSM drives with tight-speed regulation," *IEEE Trans. Ind. Electron.*, vol. 59, no. 12, pp. 4523–4536, Dec. 2012.
[19] D. Ding et al., "Impedance reshaping for inherent harmonics in PMSM drives with small DC-link capacitor," *IEEE Trans. Power Electron.*, vol. 37, no. 12, pp. 14265–14279, Dec. 2022.
[20] H. Li, Q. Yin, Q. Wang, H. Luo, and Y. Hou, "A novel DC-link voltage feedback active damping control method for IPMSM drives with small DC-link capacitors," *IEEE Trans. Ind. Electron.*, vol. 69, no. 3, pp. 2426–2436, Mar. 2022.
[21] J. H. Jung, H. J. Heo, J. M. Kim, and S. U. Choi, "DC-link voltage stabilization and source THD improvement using d-axis current injection in reduced DC-link capacitor system," in *Proc. 42nd Annu. Conf. IEEE Ind. Electron. Soc.*, Oct. 2016, pp. 2737–2742.
[22] X. Xiao, S. Zhang, Y. Ding, and Y. Song, "Control method of PMSM driving system with small DC-link capacitor," in *Proc. IEEE Energy Convers. Congr. Expo.*, Oct. 2017, pp. 1925–1931.
[23] J. Liu and Y. Zhang, "Current pulsation suppression method based on power current closed-loop control for a PMSM under fluctuating DC-link voltage," *IEEE Trans. Power Electron.*, vol. 37, no. 1, pp. 761–770, Jan. 2022.
[24] D. Wang, K. Lu, P. O. Rasmussen, L. Mathe, Y. Feng, and F. Blaabjerg, "Voltage modulation using virtual positive impedance concept for active damping of small DC-link drive system," *IEEE Trans. Power Electron.*, vol. 33, no. 12, pp. 10611–10621, Dec. 2018.
[25] Y. Son and J.-I. Ha, "Direct power control of a three-phase inverter for grid input current shaping of a single-phase diode rectifier with a small DC-link capacitor," *IEEE Trans. Power Electron.*, vol. 30, no. 7, pp. 3794–3803, Jul. 2015.
[26] H. Shin, Y. Son, and J.-I. Ha, "Grid current shaping method with DC-link shunt compensator for three-phase diode rectifier-fed motor drive system," *IEEE Trans. Power Electron.*, vol. 32, no. 2, pp. 1279–1288, Feb. 2017.
[27] R. Gao, G. Wang, G. Zhang, Z. Ren, and D. Xu, "Active damping control strategy with power analysis for reduced DC-link capacitance PMSM drives," in *Proc. 31st Int. Symp. Ind. Electron.*, Jun. 2022, pp. 468–473.
[28] K. Li, T. Sun, H. Li, Y. Wang, W. Li, and L. Gong, "Grid current quality improvement for three-phase diode rectifier-fed small DC-link capacitance IPMSM drives," *IEEE Trans. Energy Convers.*, vol. 37, no. 4, pp. 2310–2320, Dec. 2022.
[29] R. Maheshwari, S. Munk-Nielsen, and K. Lu, "An active damping technique for small DC-link capacitor based drive system," *IEEE Trans. Ind. Inform.*, vol. 9, no. 2, pp. 848–858, May 2013.
[30] L. Mathe, L. Török, D. Wang, and D. Sera, "Resonance reduction for ac drives with small capacitance in the DC link," *IEEE Trans. Ind. Appl.*, vol. 53, no. 4, pp. 3814–3820, Jul./Aug. 2017.
[31] Y. Yu, Y. Shao, F. Chai, and M. Cui, "Static-errorless position estimation for sensorless PMSM drives with enhanced robustness against the full-frequency domain disturbance," *IEEE Trans. Power Electron.*, vol. 37, no. 5, pp. 5884–5897, May 2022.
[32] G. Zhang et al., "Hybrid pseudorandom signal injection for position sensorless SynRM drives with acoustic noise reduction," *IEEE Trans. Transp. Electrific.*, vol. 8, no. 1, pp. 1313–1325, Mar. 2022.

Dawei Ding (Member, IEEE) received the B.S. and M.S. degrees in electrical engineering from Hefei University of Technology, Hefei, China, in 2014 and 2017, respectively, and the Ph.D. degree in electrical engineering from Harbin Institute of Technology (HIT), Harbin, China, in 2021.

He is currently an Assistant Professor with the School of Electrical Engineering and Automation, HIT. From 2020 to 2021, he was a Visiting Ph.D. Student with the Technical University of Denmark. He has authored more than 30 journal papers in IEEE Transactions and held tens of authorized Chinese invention patents. His research interests include advanced control of permanent magnet synchronous motor drives and electrolytic capacitorless ac motor drives.

Hui Xie received the B.S. degree in electrical engineering from Hefei University of Technology, Hefei, China, in 2022. He is currently working toward the M.S. degree in power electronics and electrical drives with the Harbin Institute of Technology, Harbin, China.

His current research focuses on advanced control strategies for electrolytic capacitorless drives.

Binxing Li (Member, IEEE) received the B.S. degree in electrical engineering from the Harbin Institute of Technology (HIT), Weihai, China, in 2017, and the Ph.D. degree in electrical engineering from the HIT, Harbin, China, in 2022.

He is currently a Postdoctor with the School of Electrical Engineering and Automation, HIT. His research interests include permanent magnet synchronous motor drives, high efficiency ac–dc converter, and application of GaN power devices.

Gaolin Wang (Senior Member, IEEE) received the B.S., M.S., and Ph.D. degrees in electrical engineering from Harbin Institute of Technology, Harbin, China, in 2002, 2004, and 2008, respectively.

In 2009, he joined, as a Lecturer, the Department of Electrical Engineering, Harbin Institute of Technology, where he has been a Full Professor of electrical engineering since 2014. From 2009 to 2012, he was a Postdoctoral Fellow with the Shanghai Step Electric Corporation. He has authored more than 70 technical papers published in IEEE Transactions. He is the holder of 40 Chinese patents. His research interests include permanent magnet synchronous motor drives and power converters.

Dr. Wang is a Guest Associate Editor for IEEE TRANSACTIONS ON INDUSTRIAL ELECTRONICS, and an Associate Editor for IEEE TRANSACTIONS ON TRANSPORTATION ELECTRIFICATION and *IET Electric Power Applications*.

Runfeng Gao received the B.S. and M.S. degrees in electrical engineering, in 2020 and 2022, respectively, from Harbin Institute of Technology, Harbin, China, where he is currently working toward the Ph.D. degree in power electronics and electrical drives.

His research interests include advanced control strategies for PMSM system and electrolytic capacitorless drives.

Zekun Ren received the B.S. degree in electrical engineering and automation from Northeast Agricultural University, Harbin, China, in 2020, and the M.S. degree in electrical engineering, in 2022, from Harbin Institute of Technology, Harbin, where he is currently working toward the Ph.D. degree in power electronics and electrical drives with the School of Electrical Engineering and Automation.

His current research focuses on electrolytic capacitorless motor drives.

Weixin Yue received the B.S. degree in electrical engineering from the Harbin Institute of Technology (HIT), Weihai, China, in 2021, and the M.S. degree in electrical engineering, in 2023, from HIT, Harbin, China, where he is currently working toward the Ph.D. degree in power electronics and electrical drives with the School of Electrical Engineering and Automation.

His current research focuses on the electrolytic capacitorless permanent magnet synchronous motor drives.

Dianguo Xu (Fellow, IEEE) received the B.S. degree in control engineering from Harbin Engineering University, Harbin, China, in 1982, and the M.S. and Ph.D. degrees in electrical engineering from Harbin Institute of Technology (HIT), Harbin, in 1984 and 1989, respectively.

In 1984, he joined the Department of Electrical Engineering, HIT, as an Assistant Professor. Since 1994, he has been a Professor with the Department of Electrical Engineering, HIT. From 2000 to 2010, he was the Dean of School of Electrical Engineering and Automation, HIT. From 2014 to 2020, he was the Vice President of HIT. He has authored/coauthored more than 600 technical papers. His research interests include renewable energy generation technology, power quality mitigation, sensorless vector controlled motor drives, and high-performance servo system.

Dr. Xu is a Chairman of IEEE Harbin Section, Co-EIC for IEEE TRANSACTIONS ON POWER ELECTRONICS, and an Associate Editor for IEEE TRANSACTIONS ON INDUSTRIAL ELECTRONICS and IEEE JOURNAL OF EMERGING AND SELECTED TOPICS IN POWER ELECTRONICS. He was the recipient of the 2018 IEEE IAS Outstanding Achievement Award.